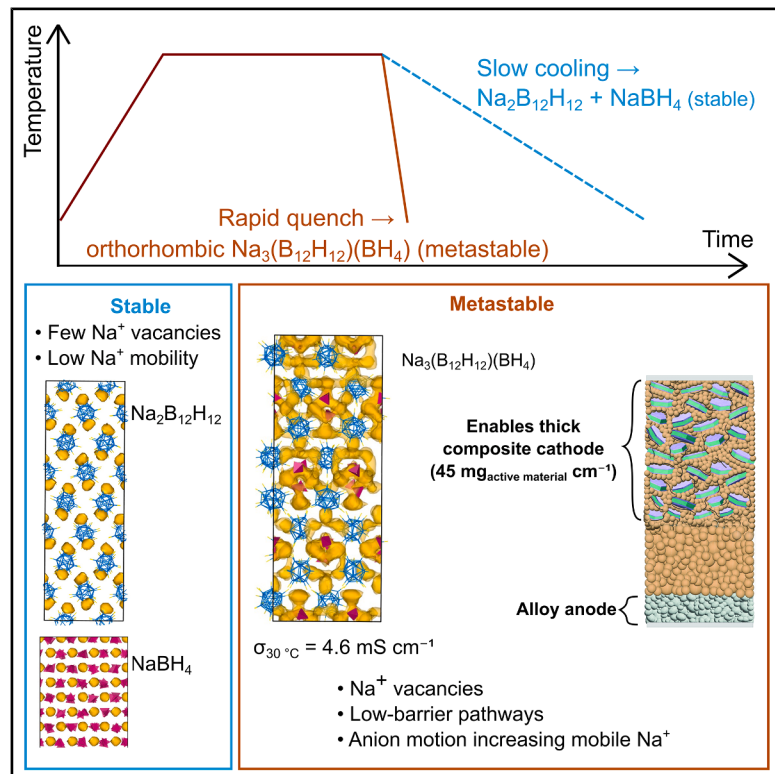


# Metastable sodium closo-hydridoborates for all-solid-state batteries with thick cathodes

## Graphical abstract



## Authors

Jin An Sam Oh, Zihan Yu,  
Chen-Jui Huang, ..., Kent J. Griffith,  
Shyue Ping Ong, Ying Shirley Meng

## Correspondence

k3griffith@ucsd.edu (K.J.G.),  
ongsp@ucsd.edu (S.P.O.),  
shirleymeng@uchicago.edu (Y.S.M.)

## In brief

Most sodium solid electrolytes still lack high room-temperature ionic conductivity needed to compete with established lithium systems. Here, a metastable orthorhombic sodium hydridoborate solid electrolyte is stabilized by rapid cooling, achieving an ionic conductivity of  $4.6 \text{ mS cm}^{-1}$  at  $30^\circ\text{C}$ . In the cathode composite, the enhanced  $\text{Na}^+$  kinetics enable a high  $45 \text{ mg}_{\text{active material}} \text{ cm}^{-2}$  cathode loading with high reversible capacity.

## Highlights

- Stabilizing metastable orthorhombic sodium hydridoborate solid electrolyte
- Cluster anion motions increase the mobile  $\text{Na}^+$  population
- Improved  $\text{Na}^+$  kinetic enables  $45 \text{ mg}_{\text{active material}} \text{ cm}^{-2}$  cathode loading
- Sn/ $\text{NaCrO}_2$  cell exhibits high reversible capacity of  $>3 \text{ mAh cm}^{-2}$

Article

# Metastable sodium closo-hydridoborates for all-solid-state batteries with thick cathodes

Jin An Sam Oh,<sup>1,2,8</sup> Zihan Yu,<sup>1,8</sup> Chen-Jui Huang,<sup>3</sup> Phillip Ridley,<sup>1</sup> Alex Liu,<sup>1</sup> Tianren Zhang,<sup>4</sup> Bing Joe Hwang,<sup>5,6</sup> Kent J. Griffith,<sup>4,\*</sup> Shyue Ping Ong,<sup>1,7,\*</sup> and Ying Shirley Meng<sup>1,3,7,9,\*</sup>

<sup>1</sup>Aiiso Yufeng Li Family Department of NanoEngineering, University of California, San Diego, La Jolla, CA 92093, USA

<sup>2</sup>Institute of Materials Research and Engineering (IMRE), Agency for Science, Technology and Research (A\*STAR), Singapore 138634, Singapore

<sup>3</sup>Pritzker School of Molecular Engineering, The University of Chicago, Chicago, IL 60637, USA

<sup>4</sup>Department of Chemistry, University of California, San Diego, La Jolla, CA 92093, USA

<sup>5</sup>NanoElectrochemistry Laboratory, Department of Chemical Engineering, Sustainable Electrochemical Energy Development Center, National Taiwan University of Science and Technology, Taipei City 106, Taiwan

<sup>6</sup>National Synchrotron Radiation Research Center, Hsinchu 30076, Taiwan

<sup>7</sup>Energy Storage Research Alliance, Argonne National Laboratory, Lemont, IL 60637, USA

<sup>8</sup>These authors contributed equally

<sup>9</sup>Lead contact

\*Correspondence: [k3griffith@ucsd.edu](mailto:k3griffith@ucsd.edu) (K.J.G.), [ongsp@ucsd.edu](mailto:ongsp@ucsd.edu) (S.P.O.), [shirleymeng@uchicago.edu](mailto:shirleymeng@uchicago.edu) (Y.S.M.)

<https://doi.org/10.1016/j.joule.2025.102130>

**CONTEXT & SCALE** All-solid-state batteries (ASSBs) potentially offer a higher energy density and improved safety relative to liquid-electrolyte systems, but progress depends on solid electrolytes with high ionic conductivity and good compatibility with composite cathodes. To address the lithium resource limits, sodium chemistries are attractive, yet sodium solid electrolytes show limited room-temperature ionic conductivity. This work combines computational and experimental data to evaluate the metastability of a sodium hydridoborate and show that rapid cooling from the crystallization regime kinetically locks the orthorhombic phase with fast Na<sup>+</sup> mobility. When paired with a chloride-based solid-electrolyte-coated cathode, this metastable phase enables thick, high-areal-loading composite cathodes that retain performance down to subzero temperatures. Because the underlying principle is kinetic stabilization of a diffusion-favorable anion framework, this approach is transferable to related hydridoborates and other anion-cluster chemistries. This work provides a practical design strategy and processing guidelines for high-performing solid electrolytes.

## SUMMARY

All-solid-state batteries (ASSBs) featuring a thick cathode layer paired with a high-capacity alloy anode offer enhanced energy density and reliable performance, even at subzero temperatures, and can outperform their liquid-based counterparts. Enabling such technology requires a solid electrolyte with high ionic conductivity, mechanical formability, and excellent electrochemical stability. Here, we demonstrate that a kinetically stable orthorhombic Na<sub>3</sub>(B<sub>12</sub>H<sub>12</sub>)(BH<sub>4</sub>) phase exhibits a superionic conductivity of 4.6 mS cm<sup>-1</sup> at 30°C alongside excellent reduction stability. High-throughput molecular dynamic simulations reveal that the propensity for anion motion significantly enhances the population of highly mobile Na<sup>+</sup> without affecting the activation energy. By leveraging its high conductivity across a wide temperature range, this material enables the development of all-solid-state sodium-ion batteries with ultra-thick cathodes, delivering reliable functionality at room temperature and in subzero environments. This study expands our understanding of hydridoborate-based solid electrolytes, highlighting their potential in next-generation energy storage systems.

## INTRODUCTION

All-solid-state batteries (ASSBs), with a solid electrolyte replacing the liquid electrolyte in conventional batteries, have attracted considerable attention in academia and industry because of their

promising intrinsic characteristics, including enhanced safety, longer life cycle, and high energy density.<sup>1,2</sup> While lithium-based batteries remain the dominant technology, sodium-based ASSBs are a complementary, safe, and cost-effective alternative chemistry owing to the abundance and cost of sodium.<sup>3,4</sup> The

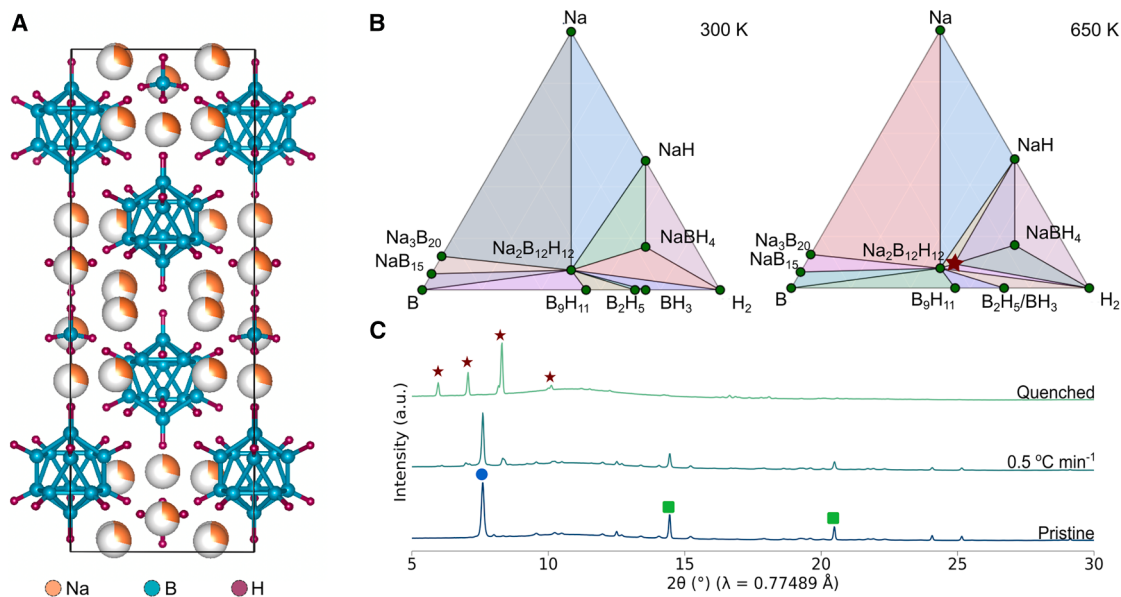


**Figure 1. Phase stability of o-NBH solid electrolyte**

(A) Crystal structure of o-NBH with partial sodium occupancy.

(B) Na-B-H compositional phase diagram based on the phonon thermodynamic properties. The calculated stable phases are indicated by the green dot, and o-NBH is indicated by **★**.

(C) Room-temperature XRD pattern of o-NBH with different cooling rates (**★**, o-NBH<sup>24</sup>; **●**, Na<sub>2</sub>B<sub>12</sub>H<sub>12</sub> [ICSD 164649]; and **■**, NaBH<sub>4</sub> [ICSD 182734]).

general rule in the selection of optimal solid electrolytes depends on several factors: ionic conductivity, electrochemical and chemical stability, and mechanical properties.<sup>5,6</sup>

Owing to poor sodium diffusivity and high Young's modulus of oxide cathodes, a solid electrolyte must be integrated with the active material to provide ionic percolation in the electrode layer. Thus, solid electrolytes must possess low modulus to conform effectively to the cathode while preserving the intimate contact between the materials during repeated electrochemical reactions. For the ASSBs to displace conventional lithium-ion (Li-ion) batteries, a thick and dense cathode, along with the use of a high-capacity alloy anode, is necessary to enhance the energy density at the cell level.<sup>2,7</sup> Accordingly, a highly conductive (>mS cm<sup>-1</sup>) solid electrolyte is highly sought after to minimize ohmic resistance and polarization in battery cells.

Sodium hydridoborates are promising solid electrolytes owing to their low density (~1.2 g cm<sup>-3</sup>), low toxicity, excellent reduction stability, and moderately soft mechanical properties, which enable densification at room temperature.<sup>8–12</sup> Reports show that incorporating mixed alio- or isovalent anions compounds can stabilize the high-symmetry polymorph (Table S1), leading to superionic conductivity at room temperature.<sup>13–19</sup> While the highly symmetric anion structure supports long-range Na<sup>+</sup> diffusion, its regular coordination sites create a large energy gap that hinders Na<sup>+</sup> migration.<sup>20,21</sup> In contrast, lowering the anion-lattice symmetry creates irregular coordination environment, reducing energy barriers and enhancing ionic conductivity.<sup>22,23</sup>

Despite these potential benefits, the orthorhombic sodium closo-hydridoborate with *Cmc2<sub>1</sub>* symmetry (o-NBH, with a chemical composition of Na<sub>3</sub>(B<sub>12</sub>H<sub>12</sub>)(BH<sub>4</sub>)) (Figure 1A) exhibits

one order of magnitude lower room-temperature ionic conductivity, compared with phases where the anions retain a high-symmetry backbone.<sup>24</sup> The uncertain thermostability of the o-NBH at room temperature may lead to degradation or phase transitions, potentially reducing the purity of the synthesized material. In this work, we combine experimental and computational approaches to demonstrate that metastable o-NBH exhibits superionic conductivity, reaching 4.6 mS cm<sup>-1</sup> at 30°C. This material facilitates the development of ASSBs with an ultra-thick cathode (approximately 310 μm), which deliver reliable capacity not only at room temperature but also in subzero environments.

## RESULTS AND DISCUSSION

### Synthesis and structure analysis

The phase diagrams of Na-B-H in Figure 1B, derived from highly accurate high-throughput density function theory (DFT) calculations (see methods), suggest that o-NBH is not thermodynamically stable with energy above hull of 16 meV atom<sup>-1</sup> at 300 K, but it is entropically stabilized at temperatures above 650 K. Differential scanning calorimetry (DSC) and synchrotron X-ray diffraction (s-XRD) patterns were collected to determine the phase evolution with temperature. DSC and *in situ* XRD in Figures S1A and S1B, respectively, show that the formation of the o-NBH phase begins at approximately 360°C and is fully formed at 400°C. After the formation of o-NBH, rapid cooling of the material by quenching the glass capillary in 25°C water leads to only the o-NBH phase without any observable precursor reflections (Figures 1C and S1C). However, a slow cooling rate (0.5°C min<sup>-1</sup>) from 400°C to room temperature leads to a mixture

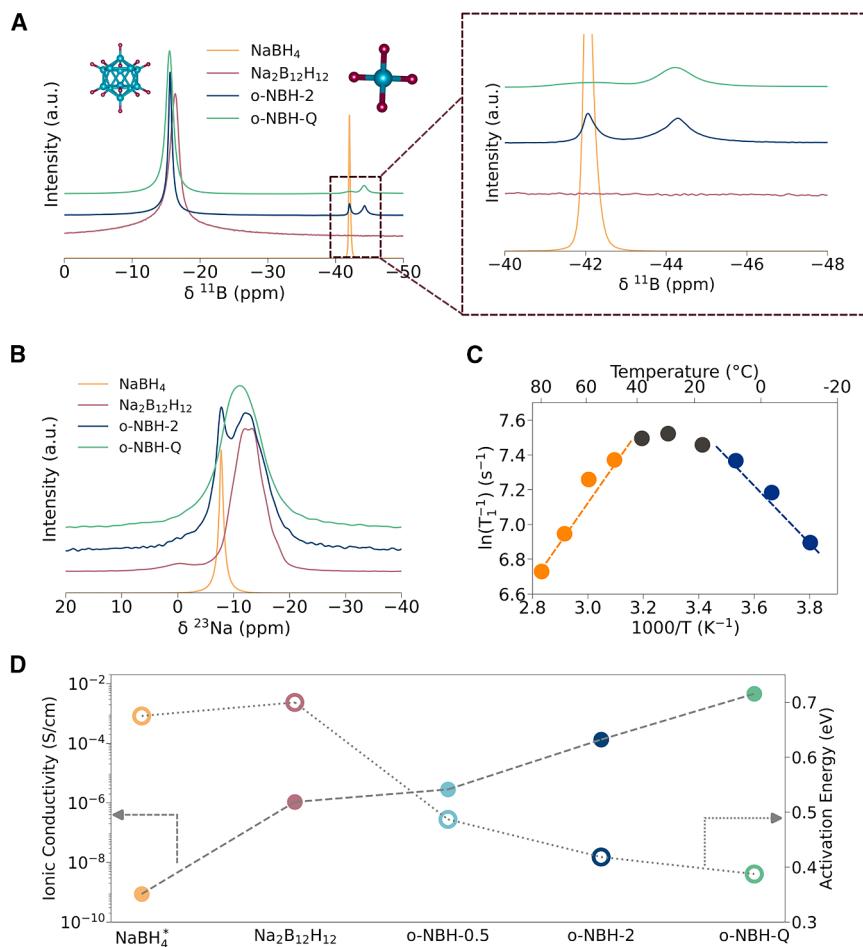


**Figure 2. Local environment and ionic conductivity of o-NBH prepared with different cooling rates**

(A and B) (A)  $^{11}\text{B}$  and (B)  $^{23}\text{Na}$  ss-NMR spectra of the precursors, o-NBH-2, and o-NBH-Q.

(C) Arrhenius behavior of the  $^{23}\text{Na}$  spin-lattice relaxation at variable temperatures.

(D) Ionic conductivity at 30°C and activation energy of o-NBH prepared with different cooling rates ( $0.5, 2^\circ\text{C min}^{-1}$ , and Ar-gas quenching) and reported values.<sup>16,24</sup>

ters are mixed into a single phase at the atomic scale comes from two-dimensional  $^1\text{H}$ - $^1\text{H}$  dipolar-coupling-mediated spin-exchange spectra (Figure S2), which shows strong correlations even at millisecond mixing times. Of great utility is that the distinct chemical shifts of  $^{11}\text{BH}_4$  in o-NBH vs.  $\text{NaBH}_4$  allow us to directly estimate the fraction of the o-NBH phase to be 90 atom % when quenched vs. 61 atom % when cooled at  $2^\circ\text{C min}^{-1}$ .

Additionally,  $^{23}\text{Na}$  NMR spectra (Figure 2B) indicates the existence of two distinct sodium environments in o-NBH-2, which match  $\text{NaBH}_4$  and  $\text{Na}_2\text{B}_{12}\text{H}_{12}$  at  $-7.8$  and  $-12.1$  ppm, respectively. On the other hand, o-NBH-Q shows a single resonance centered at  $-11.2$  ppm, indicating that there is a chemical exchange and shift averaging between the two environments,<sup>27</sup> which is expected in the pro-

posed structure model featuring neighboring  $\text{B}_{12}\text{H}_{12}$  and  $\text{BH}_4$  clusters with rapid  $\text{Na}^+$  dynamics. The  $^{23}\text{Na}$  line shapes thus support the metastable nature of the o-NBH phase, which is kinetically stabilized at room temperature by rapid cooling. Moreover,  $^{23}\text{Na}$  spin-lattice relaxation, which is dominated by fluctuating quadrupolar interactions stimulated by ionic motion in diamagnetic sodium closo-hydridoborate, is enhanced by four orders of magnitude in o-NBH-Q ( $T_1 = 0.56$  ms) relative to the precursors (Table S3). This magnitude of increased relaxation rate is indicative of rapid  $\text{Na}^+$  mobility in o-NBH, as seen in other families of sodium superionic conductors.<sup>28-31</sup>

Variable temperature spin-lattice relaxation (VT-SLR) of the  $^{23}\text{Na}$  was measured to obtain the local dynamics of  $\text{Na}^+$  in o-NBH-Q.<sup>32,33</sup> Two activation energies can be obtained from VT-SLR (Figure 2C); the short-range correlations or localized diffusion is considered for low temperature where  $\omega_0\tau \gg 1$  holds, while longer-range correlations are considered for high temperature where  $\omega_0\tau \ll 1$  holds.<sup>34,35</sup> The short-range and long-range activation energies calculated from VT-SLR are 0.13 and 0.23 eV, respectively, which are lower than the cubic  $\text{Na}_4(\text{B}_{12}\text{H}_{12})(\text{B}_{10}\text{H}_{10})$  phase, exhibiting hopping barriers of 0.19 and 0.33 eV, respectively,<sup>36</sup> indicating a lower  $\text{Na}^+$  migration barrier in the o-NBH-Q phase reported here. According to the Bloembergen, Purcell, and Pound (BPP) model ( $E_a^{\text{LT}} = (\beta - 1)$

of  $\text{Na}_2\text{B}_{12}\text{H}_{12}$  and  $\text{NaBH}_4$ , implying that o-NBH is a metastable phase that dissociates into its enthalpy-preferred precursors if given sufficient energy and time.

The local environments of the materials prepared with different cooling rates (denoted o-NBH-2 and o-NBH-Q with  $2^\circ\text{C min}^{-1}$  cooling and quenching of o-NBH, respectively) were further probed using  $^{11}\text{B}$ ,  $^1\text{H}$ , and  $^{23}\text{Na}$  solid-state nuclear magnetic resonance (ss-NMR) spectroscopy. The  $^{11}\text{B}$  ss-NMR spectra of  $\text{Na}_2\text{B}_{12}\text{H}_{12}$  and  $\text{NaBH}_4$  in Figure 2A each exhibits a single resonance with chemical shifts of  $-16.3$  and  $-42.1$  ppm, respectively.<sup>25,26</sup> o-NBH-Q has two resonances centered at  $-15.5$  and  $-44.3$  ppm, which are attributed to boron in  $\text{B}_{12}\text{H}_{12}$  and  $\text{BH}_4$  clusters, respectively. The similarity between  $^{11}\text{B}$  spectra in the precursors and o-NBH phase suggests that the  $\text{B}_{12}\text{H}_{12}$  and  $\text{BH}_4$  clusters are maintained after thermal treatment but with differentiated neighboring sodium distributions. The more negative chemical shift of  $^{11}\text{BH}_4$  in o-NBH ( $-44.3$  ppm) vs. in  $\text{NaBH}_4$  ( $-42.1$  ppm) is attributed to electron density donated by the additional  $\text{Na}^+$  from the  $\text{Na}_2\text{B}_{12}\text{H}_{12}$  component around the more localized (harder)  $\text{BH}_4$  group in the o-NBH structure. Consequently, the  $^{11}\text{B}_{12}\text{H}_{12}$  exhibits a more positive chemical shift from  $-16.3$  to  $-15.5$  ppm. This hypothesis is supported by Cambridge Serial Total Energy Package (CASTEP) calculations (Table S2). Strong evidence that the  $\text{B}_{12}\text{H}_{12}$  and  $\text{BH}_4$  clus-

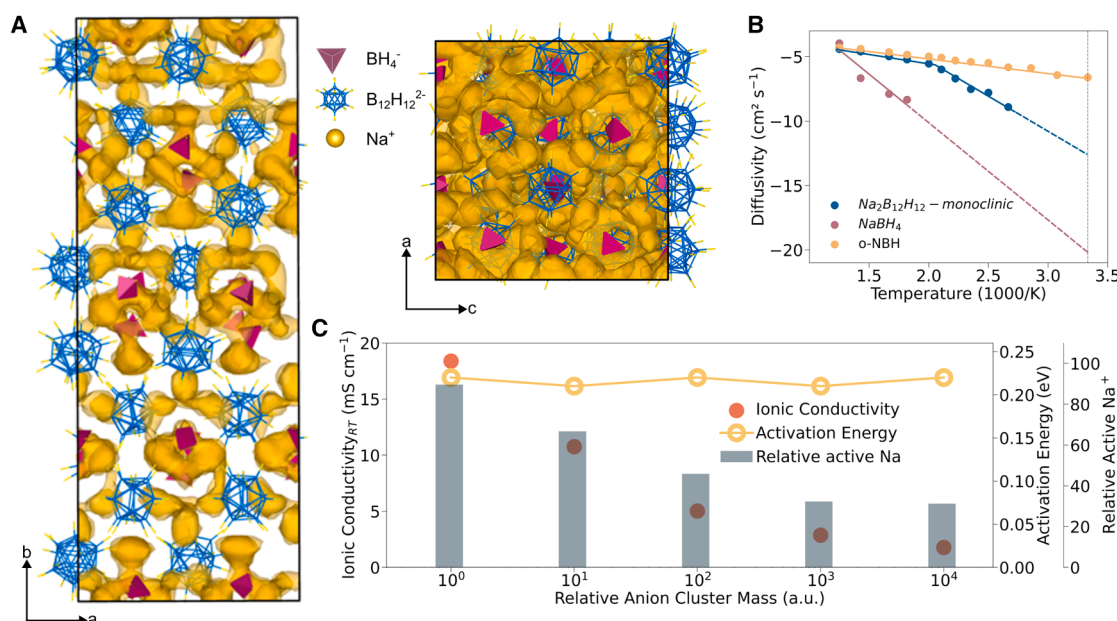


**Figure 3. o-NBH crystal structure and ionic diffusion mechanism**

(A) Iso-surface of the Na-probability density function (threshold = 0.5 Å) obtained from 2 ns MD simulation at 300 K. The  $\text{BH}_4^-$  and  $\text{B}_{12}\text{H}_{12}^{2-}$  anions are shown as fixed red and blue polyhedral, respectively.

(B) Arrhenius plots of diffusivity vs. temperature for NBH structures.

(C) Computed room-temperature 300 K ionic conductivity, activation energy, and relative active  $\text{Na}^+$  with higher anion-cluster mass.

$E_a^{\text{HT}}$ ,  $\beta$  being a measure of the strength of correlation with simple BPP behavior),<sup>36–38</sup> a  $\beta$  value of 1.54 indicates uncorrelated  $\text{Na}^+$  motion that stems from coulomb interactions and/or structural disorder, which will be revisited computationally (*vide infra*). Furthermore, at maximum SLR ( $T_{\text{max}}$  temperature, 30°C) where  $\tau\omega_0 \sim 1$  holds, a jump rate ( $1/\tau$ ) in the order of  $10^8 \text{ s}^{-1}$  is direct evidence of the high ionic conductivity of o-NBH.

To investigate the significance of stabilizing the o-NBH on bulk  $\text{Na}^+$  diffusion, the ionic conductivity and activation energy (Figure S3) of the o-NBH prepared at different cooling rates were measured. Indeed, the ionic conductivity increases while activation energy decreases with an increasing cooling rate (Figure 2D). The ionic conductivity (at 30°C) reaches a maximum value of  $4.6 \text{ mS cm}^{-1}$  when the material was rapidly cooled, which is one of the highest among all sodium solid-state electrolytes reported (Figures S4A and S4B).<sup>39,40</sup> Direct-current polarization experiments (Figure S4C) indicate that the electronic conductivity is around  $10^{-5} \text{ mS cm}^{-1}$ , which is five orders of magnitude lower than the ionic conductivity, indicating it is highly electronically insulating. These results support that the resultant ionic conductivity highly correlates to the purity of the o-NBH, which is a function of the cooling rate used during synthesis.

### Ion diffusion mechanism

The  $\text{Na}^+$  diffusion mechanism in the o-NBH crystal structure was systematically investigated using molecular dynamic (MD) simulations with Materials 3-body Graph Network (M3GNet) graph deep learning interatomic potential (GIP). The o-NBH structure has 1/3  $\text{Na}^+$  occupancy among the seven sites in o-NBH,<sup>24</sup> and the high density of accessible sites within the structure pro-

vides multiple pathways for  $\text{Na}^+$  hopping. Additionally, o-NBH exhibits a large variation in the instantaneous coordination number of  $\text{Na-B}_{12}\text{H}_{12}$  and  $\text{Na-BH}_4$  (Figure S5) providing a flexible coordination environment and lowering the energy barrier for the fast  $\text{Na}^+$  diffusion.<sup>13</sup> Compared with  $\text{NaBH}_4$  and  $\text{Na}_2\text{B}_{12}\text{H}_{12}$ , which have no  $\text{Na}^+$  site vacancies for ion diffusion (Figure S6), the o-NBH structure exhibits a fast macroscopic three-dimensional (3D)  $\text{Na}^+$  ion diffusion network, as indicated by the yellow isosurfaces in the  $\text{Na}^+$  probability density function (Figure 3A). Beyond the intrinsic  $\text{Na}^+$  site vacancies that facilitate  $\text{Na}^+$  ion diffusion, dynamic anion motion may disrupt  $\text{Na}^+$  site ordering, further flattening the overall energy landscape.<sup>13</sup> While angular displacement exists in the anion clusters, the tracked hydrogen atom trajectory for 1 ns indicates the motion is highly randomized, which may not have a periodical promotion in the diffusion (Figure S7). Combining the high  $\text{Na}^+$  site vacancy density, low activation energy, and anion motion, o-NBH exhibits orders of magnitude higher theoretical room-temperature ionic conductivity than its monoclinic- $\text{Na}_2\text{B}_{12}\text{H}_{12}$  and cubic- $\text{NaBH}_4$  precursors (Figure 3B).

To better understand the influence of the two distinct polyanion polyhedral ( $\text{BH}_4^-$  and  $\text{B}_{12}\text{H}_{12}^{2-}$ ) in o-NBH on the  $\text{Na}^+$  diffusion dynamics, a series of thought experiment was performed by artificially scaling the mass of each type of polyanion in the MD simulations. Unlike previous works whereby anions were “frozen” in MD,<sup>41,42</sup> this approach allows for gradual adjustments to the anion rotational dynamics by modifying their moment of inertia without affecting the chemical interactions between the  $\text{Na}^+$  and anions (Figure S8). The simulations show that increasing anion mass (and decreasing anion rotation) has a

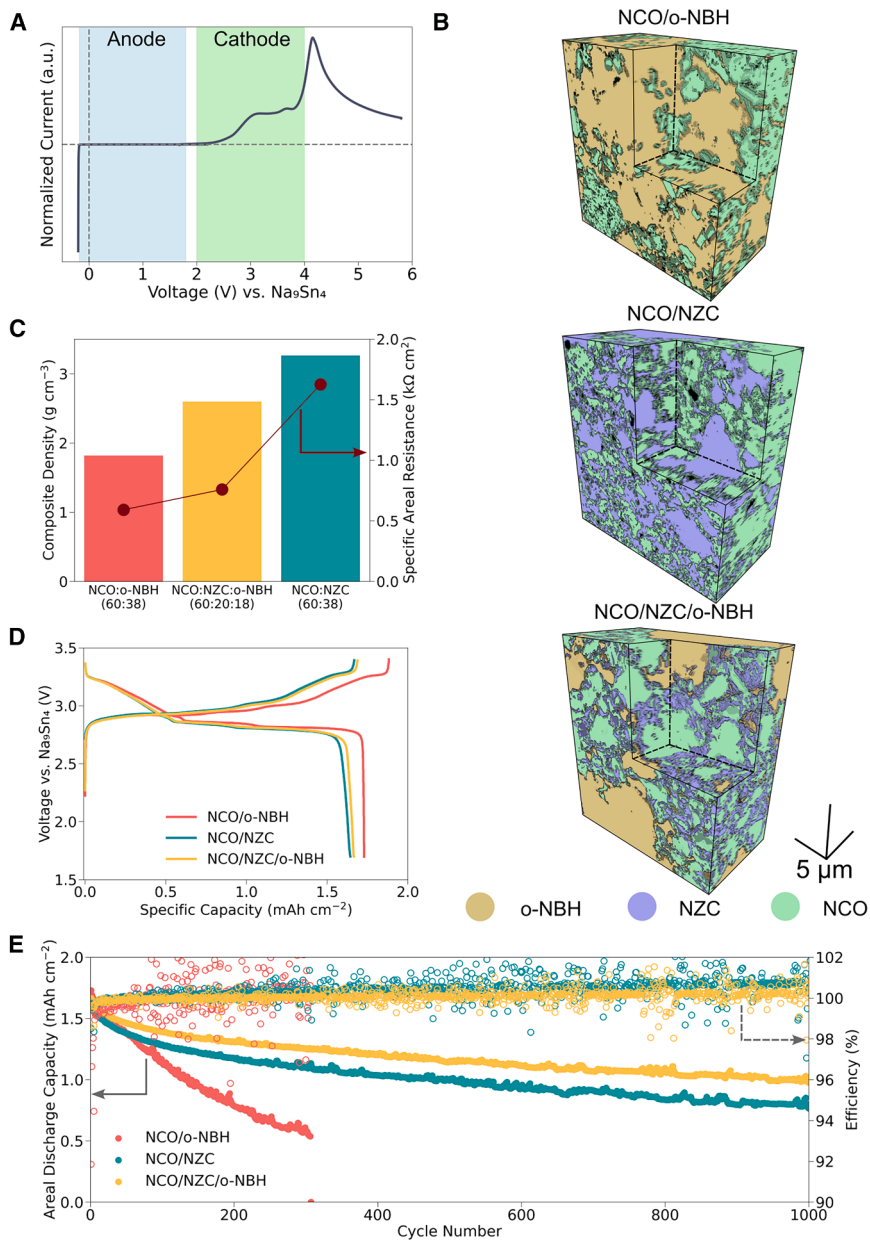


**Figure 4. Electrochemical stability of o-NBH solid electrolyte and cathode composite focused ion beam scanning electrode microscopy (FIB-SEM) tomography**

(A) LSV with a rate of  $50 \mu\text{V s}^{-1}$  of  $\text{Na}_9\text{Sn}_4//\text{o-NBH}/\text{o-NBH} + \text{additives}$  with typical electrode redox potentials highlighted (Table S5).

(B) 3D reconstructed models of NCO/NZC, NCO/o-NBH.

(C) Composite density and specific areal resistance increase with increasing NZC content due to the differences in the gravimetric density and ionic conductivity.

(D) Initial potential-capacity profiles of  $\text{Na}_9\text{Sn}_4//\text{o-NBH}/\text{NCO}$  at C/10.

(E) Reversible capacity retention of the cathode composites at C/3 in Na-excess cells with  $\text{Na}_9\text{Sn}_4$  anodes.

and energy density. Linear sweep voltammetry (LSV) indicates that the highly ionic conductive o-NBH exhibits good reduction stability against  $\text{Na}_9\text{Sn}_4$ , but limited oxidation stability, up to 2.2 V vs.  $\text{Na}_9\text{Sn}_4$  (Figure 4A). The reduction stability is further demonstrated with symmetrical  $\text{Na}_9\text{Sn}_4//\text{o-NBH}/\text{Na}_9\text{Sn}_4$  cell cycling that showed stable and reversible charge transfer after 100 cycles of  $1 \text{ mAh cm}^{-2}$  of (de)sodiation (Figure S10A).

According to the grand potential calculation at 300 K (Figure S10B), the oxidations lower than 3.8 V vs.  $\text{Na}^+/\text{Na}$  of o-NBH are hypothesized to form a passivating  $\text{Na}_2\text{B}_{12}\text{H}_{12}$ . The electrochemical oxidation is further probed by galvanostatic cycling with different maximum cut-off voltages ( $V_{\text{cutoff}}$ ) to study the implications of the various oxidation products. Initial desodiation capacities of 38 and 90  $\text{mAh g}^{-1}$  are observed with  $V_{\text{max}}$  of 3.4 and 4.9 V vs.  $\text{Na}_9\text{Sn}_4$ , respectively; negligible capacity is accessible in the subsequent cycle (Figure S10C). This is further supported by the increase in the

interfacial impedance after oxidation at 3.4 V vs.  $\text{Na}_9\text{Sn}_4$  as  $\text{Na}_2\text{B}_{12}\text{H}_{12}$  is still slightly ionically conductive (Figure S10D); a large interfacial impedance was observed after complete oxidation of o-NBH at 4.9 V vs.  $\text{Na}_9\text{Sn}_4$ .

### Sodium-excess cell (half cell)

To further evaluate the oxidation stability of o-NBH, we prepared three cathode composites:  $\text{NaCrO}_2$  with o-NBH (NCO/o-NBH), oxidation-resistant  $\text{Na-Zr-Cl}$ <sup>43</sup> solid-electrolyte-coated NCO (NCO/NZC), and NCO/NZC with o-NBH (NCO/NZC/o-NBH). The material distribution and the interfacial contact within these composites were visualized by reconstructing the cross-sectional scanning electron microscopy (SEM) images prepared by focused ion beam milling (Figure 4B). While the NCO:solid

small effect on the activation barrier for diffusion, even though there is a marked decrease in ionic conductivity (Figure 3C). Instead, the reduction in ionic conductivity is highly correlated to the reduction in the number of active  $\text{Na}^+$  with increasing anion mass. By independently modifying the  $\text{BH}_4^-$  and  $\text{B}_{12}\text{H}_{12}^-$  masses, it was found that increasing the mass of the larger  $\text{B}_{12}\text{H}_{12}^-$  anion has a more pronounced effect on the number of inactive Na and ionic conductivity (Figure S9).

### Electrochemical characterization

While high ionic conductivity is a crucial intrinsic property for a practical solid electrolyte, the electrochemical stability window impacts the viability of electrodes with high and low sodium chemical potential and, therefore, the accessible battery voltage

electrolyte:carbon mass ratio is fixed, the solid-electrolyte volume fraction is higher in o-NBH-containing composite cathode because o-NBH has a lower density ( $\sim 1.2 \text{ g cm}^{-3}$ ) than NZC ( $\sim 2.4 \text{ g cm}^{-3}$ ). Consequently, the ionic tortuosity values for NCO/o-NBH, NCO/NZC, and NCO/NZC/o-NBH are 1.53, 4.91, and 3.46, respectively. This trend correlates with the cathode composite volumetric density and impedance, where NCO/o-NBH has the lowest volumetric density and areal resistivity in the series, followed by NCO/NZC/o-NBH and then NCO/NZC (Figure 4C). The higher ionic conductivity and high volumetric content of o-NBH, compared with NZC, facilitates fast ion diffusion in the cathode composite. While such decrease in composite cathode density will lead to a decrease in the volumetric energy density (Table S6), a balance between volumetric energy density and electrochemical performance is needed for practicality.

Half-cell ASSBs were assembled using cathodes with an active material mass loading of  $15 \text{ mg}_{\text{NCO}} \text{ cm}^{-2}$  (theoretical areal capacity of  $1.8 \text{ mAh cm}^{-2}$ ) and  $\text{Na}_9\text{Sn}_4$  as the counter electrode. As shown in Figure 4D, all the cells have good material utilization (92.5%–104.2% of the theoretical NCO capacity), with the NCO/o-NBH ( $1.9 \text{ mAh cm}^{-2}$ ) cell exhibiting a slightly higher charge capacity than that of NCO/NZC ( $1.6 \text{ mAh cm}^{-2}$ ) and NCO/NZC/NBH ( $1.7 \text{ mAh cm}^{-2}$ ). In the subsequent reverse cycle, the NCO/o-NBH exhibits the lowest initial Coulombic efficiency (ICE) of 91.9%, while NCO/NZC and NCO/NZC/o-NBH have higher ICES of  $\sim 98.2\%$ . This implies that the higher-than-theoretical charge capacity in NCO/o-NBH stems from the oxidation of o-NBH. The impact of ionic tortuosity and interfacial compatibility is highlighted in the subsequent C/3 cycling. The interfacial incompatibility between NCO and o-NBH leads to rapid capacity fading as reflected by the NCO/o-NBH cell, retaining less than  $1 \text{ mAh cm}^{-2}$  ( $\sim 60\%$  of initial capacity) after 140 cycles with an average Coulombic efficiency of 99.6% (Figure 4E). Credited to the stable electrochemical interface, both NCO/NZC and NCO/NZC/o-NBH cells exhibited more stable cycling, retaining 1.23 and  $1.36 \text{ mAh cm}^{-2}$  after 140 cycles, respectively, and 0.82 and  $1.20 \text{ mAh cm}^{-2}$  after 1,000 cycles, respectively. While the first-cycle differential capacity dQ/dV plot showed similar redox reactions in each cathode-solid-electrolyte composite (Figure S11A), the NCO/o-NBH suffered from larger dQ/dV profiles polarization than that of the others (Figures S11B–S11D). Furthermore, the NCO/o-NBH cell shows a faster rate of constant-voltage capacity and an increase in cell impedance with cycle number (Figures S11E and S11F), likely fueled by the continuous formation of non-passivating and ionically insulating interphases due to o-NBH oxidation.

### Thick-cathode zero-excess-sodium cell (full cell)

For ASSBs to displace conventional Li-ion batteries, they must realize a high areal capacity using a thick cathode, minimizing inactive components at the cell level (Figures 5A and S12), and possess the ability to operate in extreme environments. This would require a high ionic conductive solid electrolyte and stable electrode/electrolyte interface. Thus, we leverage the NCO/NZC/o-NBH cathode composite architecture to assemble sodium-inventory-limited ASSBs with high-

cathode areal capacity loading (15, 30, and  $45 \text{ mg}_{\text{NCO}} \text{ cm}^{-2}$  or  $1.8, 3.6$ , and  $5.4 \text{ mAh cm}^{-2}$ , corresponding to thicknesses of approximately  $123 \pm 0.8, 217 \pm 2.6$ , and  $310 \pm 2.0 \mu\text{m}$ , respectively; Figure 5B) and Sn as the anode. While material utilization is slightly affected by the increased cathode thickness due to polarization, all cells exhibit a similar ICE (70%–81%) owing to sluggish  $\text{Na}^+$  diffusion kinetics of the Sn anode at low states of charge (SOCs), limiting the  $\text{Na}^+$  diffusion at the 2D electrode/electrolyte interface (Figures 5C, S13, and S14). Nevertheless, the ASSBs still deliver high reversible capacities of 1.3, 2.2, and  $3.5 \text{ mAh cm}^{-2}$  at 15, 30, and  $45 \text{ mg}_{\text{NCO}} \text{ cm}^{-2}$  loadings, respectively. These are among the highest reported sodium ASSB active material areal loadings (Figure S15) and feature reversible capacities that are close to or higher than conventional Li-ion batteries. Following the initial cycle, all cells have an average Coulombic efficiency of 99.8%–99.9% resulting in a capacity retention of >80% after 100 cycles (Figure 5D).

The capability of the high areal capacity cell configuration ( $45 \text{ mg}_{\text{NCO}} \text{ cm}^{-2}$ ) is further demonstrated at subzero temperatures, highlighting its viability in cold climates. The cell (Figure 5E) delivers high discharge capacities of 3.1, 2.9, 2.8, 2.5, and  $1.5 \text{ mAh cm}^{-2}$  at room temperature,  $0^\circ\text{C}$ ,  $-5^\circ\text{C}$ ,  $-10^\circ\text{C}$ , and  $-15^\circ\text{C}$ , respectively. The decrease in capacity at lower temperatures is attributed to increased cell impedance (Figure S16). Further examination of the electrochemical impedance spectra (EIS) spectra also reveals that the Warburg diffusion coefficient in the electrodes also increases significantly at  $-15^\circ\text{C}$  compared with room temperature. This suggests that the bulk diffusion in the electrode is one of the capacity-limiting factors when operating at low temperatures. Alternative electrode active materials with fast bulk diffusion at all SOC or novel electrode architecture should be considered to further improve the kinetics. Nevertheless, this work highlights that high-loading ASSBs can operate in cold climates without external heating or severe discharge capacity penalty.

### Conclusions

In conclusion, we successfully demonstrate the kinetically stable orthorhombic hydridoborate structure, o-NBH, through precise control of synthesis conditions. The lower symmetry anion framework exhibits exceptional ionic conductivity across a wide temperature range, from  $0.3 \text{ mS cm}^{-1}$  at  $-10^\circ\text{C}$  to  $4.6 \text{ mS cm}^{-1}$  at  $30^\circ\text{C}$ . Notably, the propensity of anion's motion enhances the population of highly mobile  $\text{Na}^+$ , thereby increasing the ionic conductivity, without lowering the  $\text{Na}^+$  activation energy. Incorporating o-NBH into the NCO/NZC cathode composite effectively balances the electrochemical stability with sodium-ion kinetics in the thick cathode composite. An all-solid-state sodium-ion full-cell battery with a high NCO loading ( $45 \text{ mg}_{\text{NCO}} \text{ cm}^{-2}$ ,  $\sim 310 \mu\text{m}$  thick) and Sn as cathode and anode, respectively, delivers a discharge capacity of 3.1 and  $2.5 \text{ mAh cm}^{-2}$  at room temperature and  $-10^\circ\text{C}$ , respectively. This study broadens the scope of the solid electrolyte design, extending beyond hydridoborate-based chemistry, and introduces new approaches to cell architecture that have the potential to drive the next generation of batteries.

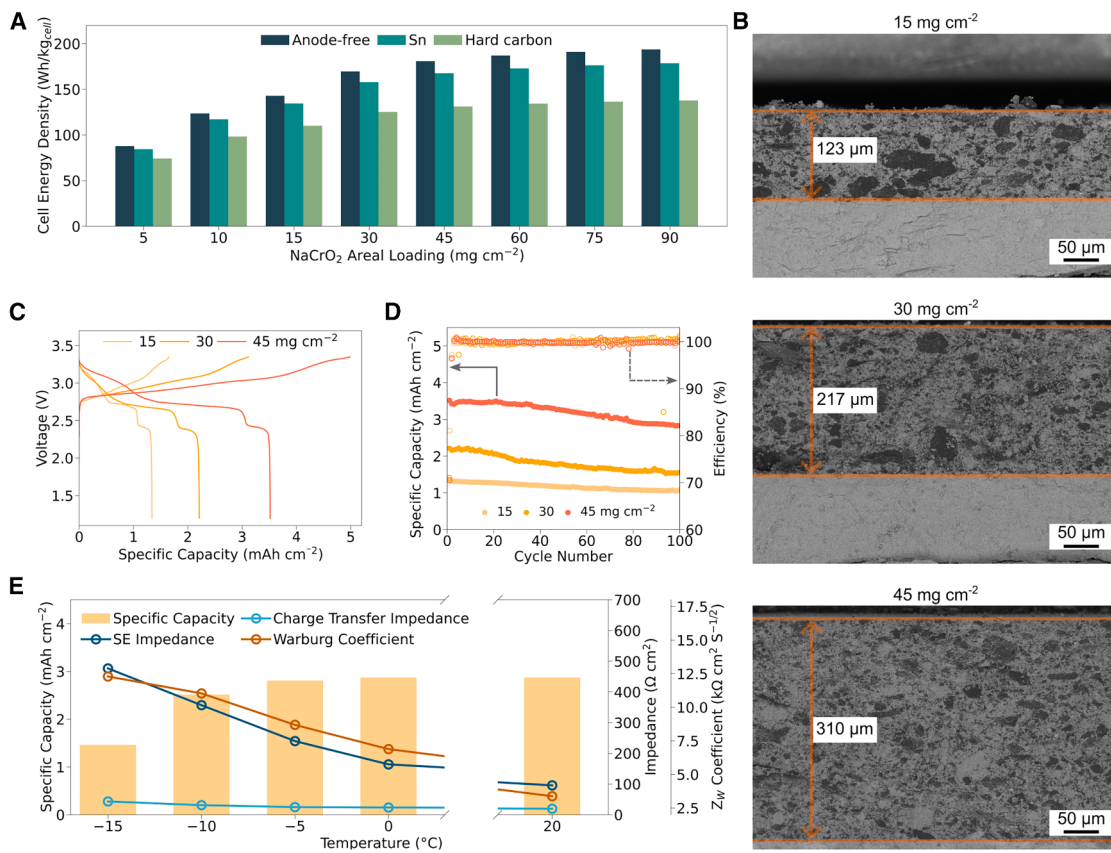


**Figure 5. Electrochemical stability of high-loading Sn//-o-NBH//NCO ASSB full cell**

- (A) Cell capacity with 50 µm NBH separator increases with increasing NCO areal loading (using 60 wt % NCO cathode composite). Detailed assumption used in the calculation can be found in [methods](#).  
 (B) Cathode thickness with various areal loadings.  
 (C) Initial potential-capacity profiles and the capacity retention with various loadings.  
 (D) Capacity retention of the full cells at C/10.  
 (E) Discharge capacity and cell impedance of a full cell with 45 mg<sub>NCO</sub> cm<sup>-2</sup> at sub-ambient temperatures.

## METHODS

### Material synthesis

All fabrication processes were conducted in an Ar-filled glovebox (H<sub>2</sub>O and O<sub>2</sub> < 5 ppm). To make the Na<sub>3</sub>(B<sub>12</sub>H<sub>12</sub>)(BH<sub>4</sub>), stoichiometric amounts of Na<sub>2</sub>B<sub>12</sub>H<sub>12</sub> (Boron Specialties LLC, dried at 175°C under dynamic vacuum for two nights) and NaBH<sub>4</sub> (99.99%, Sigma Aldrich) were hand-mixed using a pestle and mortar. Then, the mixture was sealed in a thin-wall (~0.01 mm), Boron-rich Ø0.3 mm capillary (for *in situ* s-XRD sample) or an evacuated quartz ampoule (for bulk samples). The material was heated to 410°C at 3°C min<sup>-1</sup> and held for 10 h before cooling at 0.5°C min<sup>-1</sup> and 2.0°C min<sup>-1</sup>. To achieve rapid cooling, the material was quenched in the water (for *in situ* s-XRD sample) or Ar-filled glovebox (for bulk samples) after the thermal treatment.

Na<sub>3</sub>Sn<sub>4</sub> anode was prepared by ball milling sodium metal and tin (Sn, Sigma Aldrich) using Retsch EMAX ball milling at 500 rpm for 3 h with a 30:1 Ø5 mm yttrium-stabilized zirconia ball:material weight ratio. NCO was prepared by solid-state reaction of a

pestle and mortar mixed with Na<sub>2</sub>CO<sub>3</sub> and Cr<sub>2</sub>O<sub>3</sub> at 900°C in an Ar environment for 10 h. NZC solid electrolyte was prepared by ball milling stoichiometric amounts of NaCl and ZrCl<sub>4</sub> (1:2 molar ratio)<sup>43</sup> using an Retsch EMAX ball miller at 550 rpm for 20 h with a 30:1 30:1 Ø5 mm yttrium-stabilized zirconia ball:material weight ratio.

### Materials characterization

#### Crystal structure analysis

The high-resolution s-XRD and *in situ* heating powder XRD (PXRD) were performed at beamline TPS-19A in Taiwan Photon Source (TPS), National Synchrotron Radiation Research Center (NSRRC). The energy for all PXRD was calibrated to 16 keV (0.77489 Å), with the geometry and sample position offset corrections calibrated using National Institute of Standards and Technology (NIST) standard material, LaB<sub>6</sub> (660c). A hot air gas blower was placed 2 mm under the capillary sample with a uniform ramp rate of 5°C/min for the *in situ* heating experiment. PXRD patterns were collected every 20°C along the temperature ramping process. 1D PXRD patterns

were recorded by a MYTHEN 18K detector with an exposure time of 60 s.

ss-NMR spectra were recorded under magic angle spinning (MAS) in a static magnetic field of 9.4 T with a Bruker Ascend 400 MHz magnet and a Bruker Avance NEO NMR spectrometer. The samples were packed into 1.6-mm-diameter zirconia rotors in an Ar-filled environment with polyimide and polyamide-imide caps, and spectra were measured with a Phoenix narrow-bore 1.6 mm HX probe.  $T_1$  (spin-lattice) relaxation was measured with a saturation-recovery pulse sequence for  $T_1 > 1$  s or an inversion-recovery pulse sequence for  $T_1 < 1$  s. Line broadening of  $^{11}\text{B}$  from heteronuclear dipolar coupling and J-coupling was mitigated by proton decoupling (Figure S17). All spectra were measured with a direct pulse-acquire pulse sequence using the following rf pulses:  $^{23}\text{Na}$  ( $45^\circ$ , 0.9  $\mu\text{s}$ , 135 kHz);  $^{11}\text{B}$  ( $90^\circ$ , 1.73  $\mu\text{s}$ , 145 kHz) with or without  $^1\text{H}$  decoupling (SPINAL64, 154 kHz).  $^1\text{H}$ - $^1\text{H}$  2D dipolar-coupling-mediated spin-exchange spectra (proton spin diffusion) ( $90^\circ$ , 1.36  $\mu\text{s}$ , 184 kHz) with 8 scans per row and 176 rows in the indirect dimension spaced at 50- $\mu\text{s}$  intervals were acquired with the states-time-proportional phase incrementation (TPPI) mode. Recycle delays were  $\geq 5T_1$ .

### Microstructure analysis

Owing to the moisture sensitivity, the sample was transferred from the glovebox to the SEM using the QuickLoader. The cross-section is prepared by focused Ga-ion beam milling, and SEM images were obtained using an FEI Scios DualBeam focused ion beam, equipped with an Everhart-Thornley detector. The different Z values of the NCO, NZC, and o-NBH allow a different contrast in the backscattered electron beam microscopy. The 3D reconstructed model of the composite is prepared by milling 200 nm per slice for 10  $\mu\text{m}$ . Reconstruction of the  $18 \times 20 \times 10 \mu\text{m}^3$  model is done using Thermo Scientific Avizo software. Ionic tortuosity along the z axis (separator to current collector) is calculated using the 3D reconstructed model and Tau factor in MATLAB.<sup>44</sup> The processing and imaging of the sodiated Sn was conducted at cryogenic temperature.

### Electrochemical characterization

Owing to the low modulus nature of o-NBH, the powder was pelletized at 275 MPa at room temperature (Figure S18) before electrochemical measurement. The EIS, LSV, and direct current polarization were conducted using a Biologic VSP200. To measure EIS (from 7 MHz to 1 Hz), around 90–100 mg of the materials were pelletized under a uniaxial pressure of 275 MPa. Then, acetylene black (AB) was added on both ends acting as an ion-blocking electrode before compacting at 120 MPa. The thickness of the pellet is estimated by measuring the setup before adding the powder and after the 275 MPa pelletization using a Vernier caliper. The EIS spectra at various temperatures were recorded by keeping the material under the stated temperatures ( $-10^\circ\text{C}$  to  $50^\circ\text{C}$ , at  $10^\circ\text{C}$  per step) for 1 h in an ESPEC temperature chamber.

To investigate the kinetic stability of o-NBH at room temperature, we split one batch of o-NBH-Q into two batches. One is for the immediate EIS measurement (e.g., o-NBH-Q day 0) and the other was kept in a vacuum ampoule at room temperature. Then, the EIS measurement was conducted on the kept o-NBH-Q after 30 days (e.g., o-NBH-Q day 30).

The reduction and reduction LSV sweep were conducted using o-NBH and stainless-steel powder (SS, Sigma-Aldrich) composite with a weight ratio of 1:1 and o-NBH and AB composite with a weight ratio of 7:3, respectively. Both composite electrodes were mixed using pestle and mortar and an o-NBH areal loading of  $8.9 \text{ mg cm}^{-2}$  with  $\text{Na}_9\text{Sn}_4$  as the counter electrode.

### Electrochemical characterization

**Anode preparation.** The Sn anode was prepared by casting Sn with polyvinylidene fluoride (PVDF) with a weight ratio of 99:1. The sodium-limited ASSB has a negative:positive (NP) electrode capacity ratio of 1.2–1.5, with NCO and Sn having capacities of 120 and 845 mAh g<sup>-1</sup>, respectively.

**Cathode preparation.** NCO was chosen because of its relatively low redox potential of 3.2 V vs.  $\text{Na}_9\text{Sn}_4$ , which is very close to the first oxidation of o-NBH, which is hypothesized to form the  $\text{Na}_2\text{B}_{12}\text{H}_{12}$  and  $\text{B}_2\text{H}_5$  interphases. The NCO:solid electrolyte:vapor-grown carbon fiber (VGCF) cathode composite has a mass ratio 60:38:2. The intimate contact between NCO and NZC was prepared by ball milling NCO and NZC using the PM200 at 160 rpm for 1 h (10 min of milling and 2 min of rest) with a 20:1 Ø1 mm yttrium-stabilized zirconia ball:material weight ratio. The NCO/NZC/o-NBH cathode composite has the (NCO/NZC):o-NBH:VGCF weight ratio of (60:20):18:2. All composites were hand-mixed using a pestle and mortar.

**ASSBs fabrication.** 55–60 mg of o-NBH powder was first pressed into a pellet at 275 MPa in a Ø10 mm peek sleeve using two titanium rods forming a ~540- to 620- $\mu\text{m}$ -thick solid electrolyte separator. Then, 19.6, 39.3, and 58.9 mg of the cathode composite to make 15, 30, and 45 mg<sub>NCO</sub> cm<sup>-2</sup> for a Ø10 mm cavity, respectively. Anode (35 mg of  $\text{Na}_9\text{Sn}_4$  or appropriate amount of Sn) was introduced on the other end. The cell was then pressed to 275 MPa.

**Cycling protocol.** The cells were clamped between two stainless steel plates held by bolts and nuts. For room-temperature cycling, the cells were cycled within the Ar-filled glovebox. The symmetrical  $\text{Na}_9\text{Sn}_4$ /o-NBH/ $\text{Na}_9\text{Sn}_4$  cell was cycled with a current density of  $0.2 \text{ mA cm}^{-2}$  and 5 h per half cycle (1 mAh cm<sup>-2</sup>). The half or full cells were charged with constant current-constant-voltage (CCCV) protocol, with the constant voltage set at 3.4 V and cutoff at 0.1 C (where 1 C = 120 mA g<sup>-1</sup>). The cell was contained within a homemade leakproof enclosure in the Ar-filled glovebox for low-temperature discharge performance before transferring it out. The cell was charged at  $20^\circ\text{C}$  and discharged at  $0^\circ\text{C}$ ,  $-5^\circ\text{C}$ ,  $-10^\circ\text{C}$ , and  $-15^\circ\text{C}$  in an ESPEC temperature chamber. All cells were cycled using a Landt battery cycler under an operating pressure of 75 MPa.

**Effective capacity of ASSBs.** To visualize the importance of realizing high-cathode loading cathode in battery, we calculated the estimated cell capacity considering the number of aluminum foil and solid electrolyte separators needed to achieve the target capacity. Three anodes, anode-free, Sn, and hard carbon, with a NP capacity ratio of 1.1 are considered in this illustration. Based on the previous study,<sup>9</sup> hard carbon would work well when mixed with solid electrolyte at a weight ratio of 7:3 so the mass of the hard carbon anode is corrected accordingly. The energy density

of the full cell calculation in Figure 5A is based on the following assumptions:

- (1) Aluminum current collector: 2.7 g cm<sup>-3</sup>, 20 µm.
- (2) Solid electrolyte separator: 1.3 g cm<sup>-3</sup>, 50 µm.
- (3) NP electrode ratio: 1.1.
- (4) Tin capacity: 847 mAh g<sup>-1</sup>.
- (5) Hard carbon capacity: 250 mAh g<sup>-1</sup>.
- (6) Target areal capacity: 7.2 mAh cm<sup>-2</sup>.

## Computational methods

### DFT calculations of the ss-NMR

The ss-NMR tensor calculations were carried out in the plane-wave pseudopotential code CASTEP v23.1 (Clark et al.<sup>45</sup>) on DFT-optimized structures taken from the literature.<sup>24</sup> The calculations used the Perdew-Burke-Ernzerhof exchange-correlation functional<sup>46</sup> and ultrasoft on-the-fly pseudopotentials generated in CASTEP with a plane-wave energy cutoff of 800 eV and a Monkhorst-Pack  $k$ -point grid spacing finer than  $0.04 \times 2\pi \text{ \AA}^{-1}$ .<sup>47</sup> Geometry optimization was performed with the limited-memory Broyden-Fletcher-Goldfarb-Shanno (LBFGS) algorithm<sup>48</sup> until the forces on atoms and stresses on the cell converged to better than 0.01 eV Å<sup>-1</sup> and 100 MPa, respectively. Subsequently, the NMR chemical shielding and quadrupolar interaction tensors were calculated using the gauge-including projector augmented-wave (GIPAW) approach.<sup>49-51</sup>

### Training structure generation and M3GNet training

The M3GNet architecture has already been extensively covered in previous work.<sup>52</sup> To develop a robust training data for Na-B-H M3GNet GIP, the following data generation protocol was used:

- (1) First, we extract all crystals in the Na-B-H chemical systems in Materials Project and Inorganic Crystal Structure Database (ICSD).<sup>53,54</sup> All structures were optimized with revised regularized strongly constrained and appropriately normed ( $r^2$ SCAN) functional.<sup>52</sup> The ground-state structures and relaxation trajectories (89 structures) were also included in the training dataset.
- (2) To expand the configuration space to cover more diverse local environments, particularly at higher temperatures, canonical ensemble (NVT) MD simulations were carried out using the pre-trained M3GNet universal potential<sup>52</sup> on the relaxed structures for 10 ps with a time interval of 10 fs. Simulations were also performed at 5 strains (0,  $\pm 0.05$ ,  $\pm 0.1$ ) and 5 temperatures (300–900 K with an interval of 150 K). We then sampled the snapshots using the dimensionality-reduced encoded clusters with stratified (DIRECT) sampling approach described in Qi et al.<sup>55</sup> to ensure good coverage of the configuration space.
- (3) Static self-consistent calculations with  $r^2$ SCAN functional were performed on the training structures obtained from step 2 to obtain the energies, forces, and stresses for M3GNet training. All calculations were performed with an energy cutoff of 680 eV, a  $k$  spacing of 0.35 Å<sup>-1</sup>, and an electronic relaxation convergence condition of  $1 \times 10^{-5}$  eV atom<sup>-1</sup>.<sup>56</sup>
- (4) The dataset was split into 9:1 as training and testing data-set. The radius cutoff is 5 Å and the three-body cutoff is 4 Å.

The mean absolute error (MAE) of training energies, forces, and stresses were 20.96 meV atom<sup>-1</sup>, 0.15 eV Å<sup>-1</sup>, and 1.54 meV Å<sup>-3</sup>, respectively, while the MAE of the testing set was 30.20 meV atom<sup>-1</sup>, 0.16 eV Å<sup>-1</sup>, and 1.80 meV Å<sup>-3</sup>, respectively.

All training, sampling, evaluations, and simulations with M3GNet were performed using LAMMPS,<sup>57</sup> Materials Graph Library (MatGL), and the Materials Machine Learning (maml) Python package.

### DFT calculation

All DFT calculations were performed by Vienna ab initio simulation package (VASP)<sup>58</sup> with projector augmented wave (PAW) potentials. The  $r^2$ SCAN meta-generalized gradient approximation (GGA)<sup>46</sup> functional was utilized for structural relaxation. Spin-polarized calculations with an energy cutoff of 680 eV, a  $k$  spacing of 0.35 Å<sup>-1</sup>, and an electronic relaxation convergence condition of  $1 \times 10^{-5}$  eV atom<sup>-1</sup> were applied to the structural relaxations.

### Na-B-H phase diagram calculation

The thermodynamic properties of the fixed-volume solid are estimated using phonon energies, which depend on the frequencies and the lattice internal energy from DFT calculation at 0 K. The Gibbs free energy at pressure (p), temperature (T), and volume (V) is given by  $G(V, T) = U_L(V) + U_V(V, T) - TS(V, T) + pV$ , where  $U_V(V, T)$  and  $S(V, T)$  represent the vibrational internal energy and vibrational entropy due to phonon contributions, respectively. The expressions for  $U_V$  and  $S$  are given as follows,<sup>59</sup>

$$U_V(V, T) = \sum_{\mathbf{q}, j} \hbar \omega_{\mathbf{q}, j} \left[ \frac{1}{2} + \frac{1}{\exp \left[ \frac{\hbar \omega_{\mathbf{q}, j}}{k_B T} \right] - 1} \right] \quad (\text{Equation 1})$$

$$S(V, T) = -k_B \sum_{\mathbf{q}, j} \log \left[ 1 - \exp \left( -\frac{\hbar \omega_{\mathbf{q}, j}}{k_B T} \right) \right] - \frac{1}{T} \sum_{\mathbf{q}, j} \frac{\hbar \omega_{\mathbf{q}, j}}{\exp \left[ \frac{\hbar \omega_{\mathbf{q}, j}}{k_B T} \right] - 1} \quad (\text{Equation 2})$$

where  $\omega_{\mathbf{q}, j}$  represents the phonon frequency at the wave vector  $\mathbf{q}$  and band index  $j$ . The dependence on volume is omitted for simplicity.  $k_B$  and  $\hbar$  refer to the Boltzmann constant and the reduced Planck constant, respectively.

To efficiently obtain the vibrational contributions to the entropy, phonon calculations were performed using a highly accurate M3GNet GIP fitted from a dataset of 5,595  $r^2$ SCAN calculations. Then, we calculated the Helmholtz free energies for each compound in the Na-B-H phase diagram at 300 and 650 K. The phonon thermodynamic properties were computed using the fitted Na-B-H GIP.

### Machine learning interatomic potential and MD simulations

The  $r^2$ SCAN relaxed bulk materials cubic-NaBH<sub>4</sub> (12 atoms), monoclinic-Na<sub>2</sub>B<sub>12</sub>H<sub>12</sub> (52 atoms), and o-NBH (128 atoms) were replicated by  $4 \times 4 \times 4$ ,  $4 \times 2 \times 2$ ,  $2 \times 2 \times 2$  so that all lattice parameters were larger than 10 Å. MD simulations were performed for 1 ns using pre-trained M3GNet potential at temperatures ranging from 300 to 800 K, starting with 25 K increments

from 300 to 500 K, followed by 50 K increments up to 600 K, and then increasing by 100 K from 600 to 800 K. The simulation utilized the NPT ensembles with a time step of 1 fs. All MD simulations were carried out with LAMMPS. The visualization of trajectories was achieved by OVITO. The diffusivities were extracted from the MD trajectories by using the pymatgen-analysis-diffusion package.<sup>60,61</sup>

The diffusion coefficient (D) of Na<sup>+</sup> ions was determined by applying a linear fit to the mean square displacement (MSD) vs. time (t) using the Einstein-Smoluchowski equation as follows:

$$D = \frac{\langle [\vec{r}(t+\tau) - \vec{r}(t)]^2 \rangle}{2d\tau} \quad (\text{Equation 3})$$

Where  $\vec{r}(t)$  is the position of the atom at the time  $t$ ,  $\tau$  is the time interval between atom positions  $\vec{r}(t + \tau)$  and  $\vec{r}(t)$ . The MSD is computed by  $\langle [\vec{r}(t+\tau) - \vec{r}(t)]^2 \rangle$ . Therefore, the ionic conductivity is determined by the Nernst-Einstein equation:

$$\sigma(T) = n(Ze)^2 D(T) / k_B T \quad (\text{Equation 4})$$

Where  $n$  represents the Na atom density,  $e$  is the elementary charge,  $Z$  denotes the Li-ion charge,  $k_B$  is Boltzmann's constant, and  $T$  is the absolute temperature. Activation energies ( $E_a$ ) were further determined by generating the Arrhenius plots.

The rotation speeds of B<sub>12</sub>H<sub>12</sub><sup>2-</sup> and BH<sub>4</sub><sup>-</sup> anions are artificially manipulated by proportionally increasing the cluster atomic mass. The rotation speed of each anion is determined as follows:

$$v_{rot} = \frac{\sum_0^{n_{atom}} \|[\vec{r}(t+\tau) - \vec{r}(t) - \Delta\text{com}\|}{n_{atom}R} \quad (\text{Equation 5})$$

Where  $\vec{r}(t)$  is the position of the atom at the time  $t$ ,  $\tau$  is the time interval between atom positions  $\vec{r}(t + \tau)$  and  $\vec{r}(t)$ .  $\Delta\text{com}$  is the difference in the center-of-mass position between the time steps, the Euclidean norm  $\|\cdot\|$  computes the distance,  $n_{atom}$  represents the total number of atoms, and  $R$  denotes the radius of the anions.

Estimating the active Na<sup>+</sup> ions in the o-NBH is conducted by tracing the 96 Na<sup>+</sup> ions in the structure during the simulation. Based on the [Equation 3](#) and [4](#) relationship, the average Na<sup>+</sup> MSD to achieve the 18.39 mS cm<sup>-1</sup> at 300 K is estimated to be around 21 Å<sup>2</sup>. We also noted that the MSD of H, which exhibits only rotational but no long-ranged translational motion, is around 18 Å<sup>2</sup>. Thus, we have adopted a more moderate cutoff of 21 Å<sup>2</sup> as the minimum MSD required for a Na<sup>+</sup> to be considered "active." The number of active Na<sup>+</sup> is then normalized by 96 Na<sup>+</sup> that are simulated in the calculation.

## RESOURCE AVAILABILITY

### Lead contact

Requests for further information should be directed to and will be fulfilled by the lead contact, Shirley Ying Meng ([shirleymeng@uchicago.edu](mailto:shirleymeng@uchicago.edu)).

### Materials availability

This study did not generate new unique reagents.

## Data and code availability

The DFT calculations input was generated by Pymatgen and calculated by VASP. The Na-B-H machine learning interatomic potential was trained by M3GNet that was included in MatGL (<https://github.com/materialsvirtuallab/matgl>). The MLIP-MD simulation was carried out by the interface of MatGL and Large-scale Atomic/Molecular Massively Parallel Simulator (LAMMPS) (<https://github.com/advancesoftcorp/lammps>). The diffusion analysis was conducted using pymatgen-analysis-diffusion package (<https://github.com/materialsvirtuallab/pymatgen-analysis-diffusion>).

## ACKNOWLEDGMENTS

The synchrotron radiation experiments were performed at Taiwan Photon Source (TPS), National Synchrotron Radiation Research Center (NSRRC). Electron microscopy was performed at the San Diego Nanotechnology Infrastructure (SDNI) of UCSD, a member of the National Nanotechnology Coordinated Infrastructure, which is supported by the National Science Foundation (grant no.: ECCS-2025752). J.A.S.O. is grateful for A\*STAR International Fellowship from the Agency of Science, Technology, and Research (A\*STAR). Funding: the work was supported by Energy Storage Research Alliance (DE-AC02-06CH11357), an Energy Innovation Hub funded by the US Department of Energy, Office of Science, Basic Energy Sciences. Computational work and NMR characterization at UC San Diego was supported by Shell Global Solutions Inc. (contract no. CW649697).

## AUTHOR CONTRIBUTIONS

Conceptualization, J.A.S.O. and Y.S.M.; data curation, J.A.S.O., Z.Y., C.-J.H., A.L., P.R., T.Z., and B.J.H.; formal analysis, J.A.S.O., C.-J.H., and T.Z.; investigation, J.A.S.O.; methodology, J.A.S.O., Z.Y., C.-J.H., A.L., P.R., K.J.G., and S.P.O.; writing – initial draft, J.A.S.O. and K.J.G.; validation, T.Z., K.J.G., S.P.O., and Y.S.M.; resources, B.J.H., K.J.G., S.P.O., and Y.S.M.; supervision, K.J.G., S.P.O., and Y.S.M.; writing – review and editing, S.P.O. and Y.S.M.; and all authors have provided written consent for the manuscript.

## DECLARATION OF INTERESTS

One provisional patent has been filed by University of California, San Diego Office of Innovation and Commercialization based on this work.

## DECLARATION OF GENERATIVE AI AND AI-ASSISTED TECHNOLOGIES IN THE WRITING PROCESS

During the preparation of this work, the authors used ChatGPT to assist with improving clarity and readability in certain sections of the manuscript. After using this tool/service, the authors reviewed and edited the content as needed and take full responsibility for the content of the publication.

## SUPPLEMENTAL INFORMATION

Supplemental information can be found online at <https://doi.org/10.1016/j.joule.2025.102130>.

Received: May 27, 2025

Revised: July 3, 2025

Accepted: August 21, 2025

## REFERENCES

1. Deysher, G., Oh, J.A.S., Chen, Y.-T., Sayahpour, B., Ham, S.-Y., Cheng, D., Ridley, P., Cronk, A., Lin, S.W.-H., Qian, K., et al. (2024). Design principles for enabling an anode-free sodium all-solid-state battery. Nat. Energy 9, 1161–1172. <https://doi.org/10.1038/s41560-024-01569-9>.

2. Tan, D.H.S., Meng, Y.S., and Jang, J. (2022). Scaling up high-energy-density sulfidic solid-state batteries: A lab-to-pilot perspective. Joule 6, 1755–1769. <https://doi.org/10.1016/j.joule.2022.07.002>.
3. Jakob, F., Hanicke, M., Horetsky, E., Ibrahim, D., Jautelat, S., Linder, M., Schaufuss, P., Torscht, L., and Rijt, A.v.d. (2023). Battery 2030: Resilient, Sustainable, and Circular (McKinsey & Company).
4. Hirsh, H.S., Li, Y., Tan, D.H.S., Zhang, M., Zhao, E., and Meng, Y.S. (2020). Sodium-Ion Batteries Paving the Way for Grid Energy Storage. Adv. Energy Mater. 10, 2001274. <https://doi.org/10.1002/aenm.202001274>.
5. Oh, J.A.S., He, L., Chua, B., Zeng, K., and Lu, L. (2021). Inorganic sodium solid-state electrolyte and interface with sodium metal for room-temperature metal solid-state batteries. Energy Storage Mater. 34, 28–44. <https://doi.org/10.1016/j.ensm.2020.08.037>.
6. Janek, J., and Zeier, W.G. (2023). Challenges in speeding up solid-state battery development. Nat. Energy 8, 230–240. <https://doi.org/10.1038/s41560-023-01208-9>.
7. Lewis, J.A., Cavallaro, K.A., Liu, Y., and McDowell, M.T. (2022). The promise of alloy anodes for solid-state batteries. Joule 6, 1418–1430. <https://doi.org/10.1016/j.joule.2022.05.016>.
8. Deysher, G., Chen, Y.T., Sayahpour, B., Lin, S.W.H., Ham, S.Y., Ridley, P., Cronk, A., Wu, E.A., Tan, D.H.S., Doux, J.M., et al. (2022). Evaluating Electrolyte-Anode Interface Stability in Sodium All-Solid-State Batteries. ACS Appl. Mater. Interfaces 14, 47706–47715. <https://doi.org/10.1021/acsmami.2c12759>.
9. Oh, J.A.S., Deysher, G., Ridley, P., Chen, Y.T., Cheng, D., Cronk, A., Ham, S.Y., Tan, D.H.S., Jang, J., Nguyen, L.H.B., et al. (2023). High-Performing All-Solid-State Sodium-Ion Batteries Enabled by the Presodiation of Hard Carbon. Adv. Energy Mater. 13, 2300776. <https://doi.org/10.1002/aenm.202300776>.
10. Qiu, P., Chen, X., Zhang, W., Zhang, G., Zhang, Y., Lu, Z., Wu, Y., and Chen, X. (2024). A High Rate and Long-Life Sodium Metal Battery Based on a  $\text{Na}_3\text{B}_3\text{H}_8 \cdot x\text{NH}_3$ @ $\text{Na}_3\text{B}_3\text{H}_8$  Composite Solid-State Electrolyte(224). Angew. Chem. Int. Ed. Engl. 63, e202401480. <https://doi.org/10.1002/anie.202401480>.
11. Lu, Z., Kang, J.X., Qiu, P., and Chen, X. (2025). Hydridoborate-Based Solid-State Electrolytes for Sodium Metal Batteries. Batteries Supercaps 8. <https://doi.org/10.1002/batt.202400636>.
12. Chen, X.W., Kang, J.X., Fan, Z.H., Zhang, N., Zhang, W.Y., Zhang, G.G., Zhu, A.Q., Lu, Z.W., Qiu, P., Wu, Y., et al. (2024). Sodium Octahydridotriborate as a Solid Electrolyte with Excellent Stability Against Sodium-Metal Anode. Small 20, e2401439. <https://doi.org/10.1002/smll.202401439>.
13. Kweon, K.E., Varley, J.B., Shea, P., Adelstein, N., Mehta, P., Heo, T.W., Udovic, T.J., Stavila, V., and Wood, B.C. (2017). Structural, Chemical, and Dynamical Frustration: Origins of Superionic Conductivity in closo-Borate Solid Electrolytes. Chem. Mater. 29, 9142–9153. <https://doi.org/10.1021/acs.chemmater.7b02902>.
14. Campos Dos Santos, E., Sato, R., Kisu, K., Sau, K., Jia, X., Yang, F., Orimo, S.-i., and Li, H. (2023). Explore the Ionic Conductivity Trends on  $\text{B}_{12}\text{H}_{12}$  Divalent Closot-Type Complex Hydride Electrolytes. Chem. Mater. 35, 5996–6004. <https://doi.org/10.1021/acs.chemmater.3c00975>.
15. Udovic, T.J., Matsuo, M., Unemoto, A., Verdal, N., Stavila, V., Skripov, A. V., Rush, J.J., Takamura, H., and Orimo, S. (2014). Sodium superionic conduction in  $\text{Na}_2\text{B}_{12}\text{H}_{12}$ . Chem. Commun. (Camb.) 50, 3750–3752. <https://doi.org/10.1039/c3cc49805k>.
16. Duchêne, L., Kühnel, R.S., Rentsch, D., Remhof, A., Hagemann, H., and Battaglia, C. (2017). A highly stable sodium solid-state electrolyte based on a dodeca/deca-borate equimolar mixture. Chem. Commun. (Camb.) 53, 4195–4198. <https://doi.org/10.1039/c7cc00794a>.
17. Brighi, M., Murgia, F., and Černý, R. (2020). Closot-Hydroborate Sodium Salts as an Emerging Class of Room-Temperature Solid Electrolytes. Cell Rep. Phys. Sci. 1, 100217. <https://doi.org/10.1016/j.xcrp.2020.100217>.
18. Yoshida, K., Sato, T., Unemoto, A., Matsuo, M., Ikeshoji, T., Udovic, T.J., and Orimo, S.-i. (2017). Fast sodium ionic conduction in  $\text{Na}_2\text{B}_{10}\text{H}_{10} \cdot \text{Na}_2\text{B}_{12}\text{H}_{12}$  pseudo-binary complex hydride and application to a bulk-type all-solid-state battery. Appl. Phys. Lett. 110, 103901. <https://doi.org/10.1063/1.4977885>.
19. Asakura, R., Reber, D., Duchêne, L., Payandeh, S., Remhof, A., Hagemann, H., and Battaglia, C. (2020). 4 V room-temperature all-solid-state sodium battery enabled by a passivating cathode/hydroborate solid electrolyte interface. Energy Environ. Sci. 13, 5048–5058. <https://doi.org/10.1039/D0EE01569E>.
20. Lu, Z., and Ciucci, F. (2016). Structural origin of the superionic Na conduction in  $\text{Na}_2\text{B}_{10}\text{H}_{10}$  closo-borates and enhanced conductivity by Na deficiency for high performance solid electrolytes. J. Mater. Chem. A 4, 17740–17748. <https://doi.org/10.1039/C6TA07443J>.
21. Wang, S., Fu, J., Liu, Y., Saravanan, R.S., Luo, J., Deng, S., Sham, T.K., Sun, X., and Mo, Y. (2023). Design principles for sodium superionic conductors. Nat. Commun. 14, 7615. <https://doi.org/10.1038/s41467-023-43436-3>.
22. Luo, J.D., Zhang, Y., Cheng, X., Li, F., Tan, H.Y., Zhou, M.Y., Wang, Z.W., Hao, X.D., Yin, Y.C., Jiang, B., et al. (2024). Halide Superionic Conductors with Non-Close-Packed Anion Frameworks. Angew. Chem. Int. Ed. Engl. 63, e202400424. <https://doi.org/10.1002/anie.202400424>.
23. Wang, Y., Richards, W.D., Ong, S.P., Miara, L.J., Kim, J.C., Mo, Y., and Ceder, G. (2015). Design principles for solid-state lithium superionic conductors. Nat. Mater. 14, 1026–1031. <https://doi.org/10.1038/nmat4369>.
24. Sadikin, Y., Brighi, M., Schouwink, P., and Černý, R. (2015). Superionic Conduction of Sodium and Lithium in Anion-Mixed Hydroborates  $\text{Na}_3\text{BH}_4\text{B}_{12}\text{H}_{12}$  and  $(\text{Li}_{0.7}\text{Na}_{0.3})_3\text{BH}_4\text{B}_{12}\text{H}_{12}$ . Adv. Energy Mater. 5, 1501016. <https://doi.org/10.1002/aenm.201501016>.
25. Łódziana, Z., Błoński, P., Yan, Y., Rentsch, D., and Remhof, A. (2014). NMR Chemical Shifts of 11B in Metal Borohydrides from First-Principle Calculations. J. Phys. Chem. C 118, 6594–6603. <https://doi.org/10.1021/jp4120833>.
26. Jensen, S.R.H., Paskevicius, M., Hansen, B.R.S., Jakobsen, A.S., Møller, K.T., White, J.L., Allendorf, M.D., Stavila, V., Skibsted, J., and Jensen, T.R. (2018). Hydrogenation properties of lithium and sodium hydride - closo-borate,  $[\text{B}_{10}\text{H}_{10}]^{2-}$  and  $[\text{B}_{12}\text{H}_{12}]^{2-}$ , composites. Phys. Chem. Chem. Phys. 20, 16266–16275. <https://doi.org/10.1039/c7cp07776a>.
27. Tsai, P.C., Mair, S., Smith, J., Halat, D.M., Chien, P.H., Kim, K., Zhang, D., Li, Y., Yin, L., Liu, J., et al. (2023). Double Paddle-Wheel Enhanced Sodium Ion Conduction in an Antiperovskite Solid Electrolyte. Adv. Energy Mater. 13, 2203284. <https://doi.org/10.1002/aenm.202203284>.
28. Yu, C., Ganapathy, S., de Klerk, N.J.J., van Eck, E.R.H., and Wagemaker, M. (2016). Na-ion dynamics in tetragonal and cubic  $\text{Na}_3\text{PS}_4$ , a Na-ion conductor for solid state Na-ion batteries. J. Mater. Chem. A 4, 15095–15105. <https://doi.org/10.1039/C6TA05896E>.
29. Zhou, L., Bazak, J.D., Li, C., and Nazar, L.F. (2024). 4 V Na Solid State Batteries Enabled by a Scalable Sodium Metal Oxyhalide Solid Electrolyte. ACS Energy Lett. 9, 4093–4101. <https://doi.org/10.1021/acsenergylett.4c01855>.
30. Ridley, P., Duong, G., Ko, S.L., Sam Oh, J.A.S., Deysher, G., Griffith, K.J., and Meng, Y.S. (2025). Tailoring Chloride Solid Electrolytes for Reversible Redox. J. Am. Chem. Soc. 147, 19508–19519. <https://doi.org/10.1021/jacs.4c14670>.
31. Lou, C., Zhang, W., Liu, J., Gao, Y., Sun, X., Fu, J., Shi, Y., Xu, L., Luo, H., Chen, Y., et al. (2024). The glass phase in the grain boundary of  $\text{Na}_3\text{Zr}_2\text{Si}_2\text{PO}_{12}$ , created by gallium modulation. Chem. Sci. 15, 3988–3995. <https://doi.org/10.1039/D3SC06578B>.
32. Babanova, O.A., Sadikin, Y., Skoryunov, R.V., Soloninin, A.V., and Skripov, A.V. (2024). Anion and Cation Dynamics in Mixed-Anion Hydroborate  $\text{Na}_3(\text{BH}_4)(\text{B}_{12}\text{H}_{12})$ :  $^1\text{H}$ ,  $^{11}\text{B}$ , and  $^{23}\text{Na}$  NMR Studies. Inorganics 12, 265. <https://doi.org/10.3390/inorganics12100265>.

33. Udoovic, T.J., Matsuo, M., Tang, W.S., Wu, H., Stavila, V., Soloninina, A.V., Skoryunov, R.V., Babanova, O.A., Skripov, A.V., Rush, J.J., et al. (2014). Exceptional superionic conductivity in disordered sodium decahydro-closo-decaborate. *Adv. Mater.* 26, 7622–7626. <https://doi.org/10.1002/adma.201403157>.
34. Kuhn, A., Narayanan, S., Spencer, L., Goward, G., Thangadurai, V., and Wilkening, M. (2011). Li self-diffusion in garnet-type  $\text{Li}_7\text{La}_3\text{Zr}_2\text{O}_{12}$  as probed directly by diffusion-induced  $\text{Li}^7$  spin-lattice relaxation NMR spectroscopy. *Phys. Rev. B* 83, 094302. <https://doi.org/10.1103/PhysRevB.83.094302>.
35. Ganapathy, S., Yu, C., van Eck, E.R.H., and Wagemaker, M. (2019). Peeking across Grain Boundaries in a Solid-State Ionic Conductor. *ACS Energy Lett.* 4, 1092–1097. <https://doi.org/10.1021/acsenergylett.9b00610>.
36. Duchêne, L., Lunghammer, S., Burankova, T., Liao, W.-C., Embes, J.P., Copéret, C., Wilkening, H.M.R., Remhof, A., Hagemann, H., and Battaglia, C. (2019). Ionic Conduction Mechanism in the  $\text{Na}_2(\text{B}_{12}\text{H}_{20})_{0.5}(\text{B}_{10}\text{H}_{10})_{0.5}$  closo-Borate Solid-State Electrolyte: Interplay of Disorder and Ion–Ion Interactions. *Chem. Mater.* 31, 3449–3460. <https://doi.org/10.1021/acs.chemmater.9b00610>.
37. Zhang, S., Zhao, F., Chen, J., Fu, J., Luo, J., Alahakoon, S.H., Chang, L.Y., Feng, R., Shakouri, M., Liang, J., et al. (2023). A family of oxychloride amorphous solid electrolytes for long-cycling all-solid-state lithium batteries. *Nat. Commun.* 14, 3780. <https://doi.org/10.1038/s41467-023-39197-8>.
38. Bloembergen, N., Purcell, E.M., and Pound, R.V. (1948). Relaxation Effects in Nuclear Magnetic Resonance Absorption. *Phys. Rev.* 73, 679–712. <https://doi.org/10.1103/PhysRev.73.679>.
39. Liu, G., Yang, J., Wu, J., Peng, Z., and Yao, X. (2024). Inorganic Sodium Solid Electrolytes: Structure Design, Interface Engineering and Application. *Adv. Mater.* 36, e2311475. <https://doi.org/10.1002/adma.202311475>.
40. Huang, J., Wu, K., Xu, G., Wu, M., Dou, S., and Wu, C. (2023). Recent progress and strategic perspectives of inorganic solid electrolytes: fundamentals, modifications, and applications in sodium metal batteries. *Chem. Soc. Rev.* 52, 4933–4995. <https://doi.org/10.1039/D2CS01029A>.
41. Smith, J.G., and Siegel, D.J. (2020). Low-temperature paddlewheel effect in glassy solid electrolytes. *Nat. Commun.* 11, 1483. <https://doi.org/10.1038/s41467-020-15245-5>.
42. Zhang, Z., Roy, P.N., Li, H., Avdeev, M., and Nazar, L.F. (2019). Coupled Cation–Anion Dynamics Enhances Cation Mobility in Room-Temperature Superionic Solid-State Electrolytes. *J. Am. Chem. Soc.* 141, 19360–19372. <https://doi.org/10.1021/jacs.9b09343>.
43. Wu, M., Liu, X., Liu, H., Li, D., Qi, X., Zeng, J., Gao, L., Nan, C.W., and Fan, L.Z. (2025). Fluorinated amorphous halides with improved ionic conduction and stability for all-solid-state sodium-ion batteries. *Nat. Commun.* 16, 2808. <https://doi.org/10.1038/s41467-025-58113-w>.
44. Cooper, S.J., Bertei, A., Shearing, P.R., Kilner, J.A., and Brandon, N.P. (2016). TauFactor: An open-source application for calculating tortuosity factors from tomographic data. *SoftwareX* 5, 203–210. <https://doi.org/10.1016/j.softx.2016.09.002>.
45. Clark, S.J., Segall, M.D., Pickard, C.J., Hasnip, P.J., Probert, M.I.J., Refson, K., and Payne, M.C. (2005). First principles methods using CASTEP. *Z. Kristallogr. Cryst. Mater.* 220, 567–570. <https://doi.org/10.1524/zkri.220.5.567.65075>.
46. Perdew, J.P., Burke, K., and Ernzerhof, M. (1996). Generalized Gradient Approximation Made Simple. *Phys. Rev. Lett.* 77, 3865–3868. <https://doi.org/10.1103/PhysRevLett.77.3865>.
47. Monkhorst, H.J., and Pack, J.D. (1976). Special points for Brillouin-zone integrations. *Phys. Rev. B* 13, 5188–5192. <https://doi.org/10.1103/PhysRevB.13.5188>.
48. Liu, D.C., and Nocedal, J. (1989). On the limited memory BFGS method for large scale optimization. *Math. Program.* 45, 503–528. <https://doi.org/10.1007/BF01589116>.
49. Pickard, C.J., and Mauri, F. (2001). All-electron magnetic response with pseudopotentials: NMR chemical shifts. *Phys. Rev. B* 63, 245101. <https://doi.org/10.1103/PhysRevB.63.245101>.
50. Yates, J.R., Pickard, C.J., and Mauri, F. (2007). Calculation of NMR chemical shifts for extended systems using ultrasoft pseudopotentials. *Phys. Rev. B* 76, 024401. <https://doi.org/10.1103/PhysRevB.76.024401>.
51. Profeta, M., Mauri, F., and Pickard, C.J. (2003). Accurate first principles prediction of  $^{17}\text{O}$  NMR parameters in  $\text{SiO}_2$ : assignment of the zeolite ferrierite spectrum. *J. Am. Chem. Soc.* 125, 541–548. <https://doi.org/10.1021/ja027124r>.
52. Chen, C., and Ong, S.P. (2022). A universal graph deep learning interatomic potential for the periodic table. *Nat. Comput. Sci.* 2, 718–728. <https://doi.org/10.1038/s43588-022-00349-3>.
53. Zagorac, D., Müller, H., Ruehl, S., Zagorac, J., and Rehme, S. (2019). Recent developments in the Inorganic Crystal Structure Database: theoretical crystal structure data and related features. *J. Appl. Crystallogr.* 52, 918–925. <https://doi.org/10.1107/S160057671900997X>.
54. Jain, A., Ong, S.P., Hautier, G., Chen, W., Richards, W.D., Dacek, S., Cholia, S., Gunter, D., Skinner, D., Ceder, G., et al. (2013). Commentary: The Materials Project: A materials genome approach to accelerating materials innovation. *APL Mater.* 1, 011002. <https://doi.org/10.1063/1.4812323>.
55. Qi, J., Ko, T.W., Wood, B.C., Pham, T.A., and Ong, S.P. (2024). Robust training of machine learning interatomic potentials with dimensionality reduction and stratified sampling. *npj Comp. Mater.* 10, 43. <https://doi.org/10.1038/s41524-024-01227-4>.
56. Bartók, A.P., and Yates, J.R. (2019). Regularized SCAN functional. *J. Chem. Phys.* 150, 161101. <https://doi.org/10.1063/1.5094646>.
57. Plimpton, S. (1995). Fast Parallel Algorithms for Short-Range Molecular Dynamics. *J. Comp. Phys.* 117, 1–19. <https://doi.org/10.1006/jcph.1995.1039>.
58. Kresse, G., and Furthmüller, J. (1996). Efficient iterative schemes for ab initio total-energy calculations using a plane-wave basis set. *Phys. Rev. B Condens. Matter* 54, 11169–11186. <https://doi.org/10.1103/PhysRevB.54.11169>.
59. Togo, A., and Tanaka, I. (2015). First principles phonon calculations in materials science. *Scr. Mater.* 108, 1–5. <https://doi.org/10.1016/j.scriptamat.2015.07.021>.
60. Deng, Z., Zhu, Z., Chu, I.-H., and Ong, S.P. (2017). Data-Driven First-Principles Methods for the Study and Design of Alkali Superionic Conductors. *Chem. Mater.* 29, 281–288. <https://doi.org/10.1021/acs.chemmater.6b02648>.
61. Ong, S.P., Richards, W.D., Jain, A., Hautier, G., Kocher, M., Cholia, S., Gunter, D., Chevrier, V.L., Persson, K.A., and Ceder, G. (2013). Python Materials Genomics (pymatgen): A robust, open-source python library for materials analysis. *Comp. Mater. Sci.* 68, 314–319. <https://doi.org/10.1016/j.commatsci.2012.10.028>.